Chinese Journal of Aeronautics, (2023), 36(4): 409–422

Chinese Society of Aeronautics and Astronautics
& Beihang University

Chinese Journal of Aeronautics

cja@buaa.edu.cn
www.sciencedirect.com

Control-oriented modeling of a high-aspect-ratio flying wing with coupled flight dynamics

Cong NIU [a], Xiutian YAN [a], Boyi CHEN [b,*]

[a] Department of Design, Manufacturing & Engineering Management, University of Strathclyde, Glasgow G11XQ, UK
[b] College of Astronautics, Nanjing University of Aeronautics and Astronautics, Nanjing 210016, China

Received 19 March 2022; revised 18 April 2022; accepted 21 June 2022
Available online 24 August 2022

KEYWORDS

Flexible couplings;
Flexible wings;
Flight control systems;
Flight dynamics;
Sensitivity analysis

Abstract The flight-structural dynamics of a high-aspect-ratio wing challenge the flight control design. This paper develops a reduced model of coupled dynamics with stability consideration. The structural dynamics are formulated with dihedrals, and the central loads drive the deformation. The control-oriented model with essential coupled dynamics is formulated. Modal sensitivity analysis and input–output pairing are performed to identify the control structure. Besides, an example of flight control design is provided to discuss the necessity of considering structural dynamics in controller design. Analytical coupled flight dynamics provide a system-theoretic approach for stability and facilitate model-based control techniques. Simulation results reveal the characteristics of flight-structural coupled dynamics and demonstrate that the influence of flexible modes should be considered in control design, especially in lateral dynamics.

1. Introduction

High-aspect-ratio wings are born of the trends in aerospace design to increase the global aerodynamic efficiency and reduce the structural weight to a minimum.[1] However, the failure in the flight of some research prototypes of High-Aspect-Ratio Wings (HARW) has shown that traditional methods are inadequate to fulfil the design of future aerial platforms.[2] For HARW, the flap bending mode, the chord bending mode, and the torsion mode may couple and result in significant structural nonlinearities.[1,3] van Schoor and von Flotow demonstrated that the critical issue is to include aircraft structural dynamics when analyzing aircraft flight dynamics of HARW.[4]

The flight dynamics of the deformed aircraft are significantly different from a rigid aircraft. The pair of complex-conjugate short-period roots merge to become two real roots, and the phugoid mode goes unstable when the HARW is sufficiently deformed.[5–7] The finite state two-dimensional strip theory was adopted to capture the unsteady aerodynamics.[8,9] The strain-based approach was introduced for HARW to formulate the nonlinear structural dynamics.[10] Frequencies of rigid-body motion and classic vibration tend to be close due to the considerable flexibility and the small pitching inertia.[11] Hence, it is essential to address the effects of nonlinearities on the aeroelastic behaviour of HARW.

* Corresponding author.
E-mail address: chenboyi1989@nuaa.edu.cn (B. CHEN).
Peer review under responsibility of Editorial Committee of CJA.

Production and hosting by Elsevier

https://doi.org/10.1016/j.cja.2022.08.018

HARW features very low frequencies of the natural structural vibration modes, and becomes more susceptible to higher deflection under the same operating conditions.[1] Besides, the states of flexible dynamics can be merely measured. Therefore, the flight-dynamic behaviour of such flexible aircraft contains the coupling of structural dynamics, rigid-body dynamics, and unsteady aerodynamics, which results in a high-order system.[12]

Issues in the flight control of HARW mainly include aeroelastic control for gust load alleviation and trajectory control for path following.[13–15] Many model-based control methods have been investigated,[16,17] such as H_∞ control,[18] and dynamic inversion control[19] Trajectory control of HARW requires an integrated controller that handles flexible and rigid-body motion. The design of guidance and control systems for HARW requires the control engineer to deal with strong coupling between structural and aerodynamic effects.[20]

Control designs tailored explicitly to flexible aircraft are first proposed by Gregory, where output feedback dynamic inversion techniques were modified with a pre-filter to improve the performance of the controller.[21] Raghavan and Patil presented dynamic inversion control laws where the robustness of the control designs was tested by introducing uncertainty in the mass of the aircraft.[22] A model-predictive control system is built with a quasi-steady linearized internal model.[19] Stability is significantly improved when geometrically nonlinear effects are included in the internal model of the controller. It has been demonstrated that plants with large condition numbers or relative gains are inherently sensitive to modelling uncertainties and potentially tricky to control.[23]

For model-based control methods, the control design is typically based on a mathematical model of the plant. The model order reduction is made by approximating a zero shear and zero extension.[24] Robust linear control combined with balanced truncation model-reduction methodologies was investigated for gust rejection.[25] Adaptive output-feedback control with closed-loop reference models was proposed for HARW considering model uncertainties and actuator anomalies using the balanced realization method.[26] The Proper Orthogonal Decomposition (POD) was used to obtain a low-dimensional Ordinary Differential Equation (ODE) system.[27] Above all, practical and high-fidelity model-reduction methods play an essential role in the controller design process of HARW. The model reduction simplifies the difficulty of control system design in mathematics rather than physics. Hence, the primary features of dynamics can be hardly captured.

The lagging of control design is likely to cause the scheme to fail because the dynamic coupling characteristics of the system are ignored. Control-Oriented Modelling (COM) was first introduced into the design process of a hypersonic vehicle to obtain the required performance.[28] The aim of control-oriented modelling toward developing a formulation of the reduced dynamics better suited for designing model-based controllers and assessing the theoretical properties of open-loop and closed-loop systems.[29] The necessity has been widely recognized, and several stability issues have been addressed and validated based on COM.[30,31] In addition, the modelling efforts required to complete a nonlinear design offer insight into the structure of a plant that is lost by taking a simple Jacobian linearization. To approximate the rigid-body dynamics, Gibson et al. propose a simplified design method.[32] They used fewer states to describe the influence of structure on rigid-body longitudinal dynamics, which takes the first step of control-oriented modelling for HARW. The high-fidelity models of HARW mainly focus on modelling structural dynamics with geometric nonlinearity, precisely predicting the behaviour with large deformation and discussing the flight coupling dynamics from a mechanical point of view. However, the model data for stability analysis and flight control cannot be obtained efficiently, such as stability and control derivatives.

In this paper, we aim to make the first step toward developing a formulation of the reduced dynamics better suited for designing model-based controllers and assessing the theoretical properties of open-loop and closed-loop systems. Given the successful application of control-oriented modelling in hypersonic vehicle design, we propose a control-oriented simplified model of HARW. The structural dynamics are replaced by the dynamics of dihedral angles between wings. The main contributions of this paper are summarized as follows. The control-oriented model of HARW is extended to transverse lateral motion. Reduced coupling dynamics are analytically formulated while remaining critical characteristics. The flight control structure for HARW is identified based on flight-structural coupled dynamics. Derivatives of stability and control are provided to reveal the dynamic behaviour further.

The structure of this paper is as follows: Section 2 introduces the control-oriented model of HARW; Section 3 presents some characteristics of HARW using modal sensitivity analysis and Relative Gain Array (RGA); Section 4 conducts simulation studies to test the proposed model and verify, and Section 5 concludes the paper.

2. Nonlinear flight dynamics with coupled structural dynamics

The First-Principle Model (FPM) of HARW is driven based on Newton's second theorem. To incorporate the structure dynamics, we assume that the inertia properties are dynamically dependent on the configuration, and the coupling inertial force is non-negligible. The first bending mode of the wing is approximated by the motion of dihedral angle at joints, whereas the higher-order mode of flexible dynamic is negligible.

The basic geometry of the vehicle model is illustrated in Fig. 1, which incorporates three rigid wings with elastic connections adjoining them. Each wing has a propeller, an aileron, and an elevator attached at the end of the boom. Let m denote the system's total mass, and m_i denotes the mass of the i-th wing. The centre of gravity is denoted as C, and the centre of gravity of the i-th wing is denoted as c_i. The structural dynamics are characterized by the dynamics of dihedral angles (η_1, η_3) of the joints. V denotes the velocity and P denotes the position.

Different motion parameters can describe the movement of the aircraft. Generally speaking, the dynamic equations of aircraft are derived from the body coordinate system. However, the calculations of aerodynamic forces and moments require information on the aerodynamic angle. For this reason, to make the model closed, the flight velocity V, the angle of attack α and the sideslip angle β are chosen to be the states rather than the components of $\boldsymbol{V}^{\mathbf{B}} = [u, v, w]^{\mathrm{T}}$.

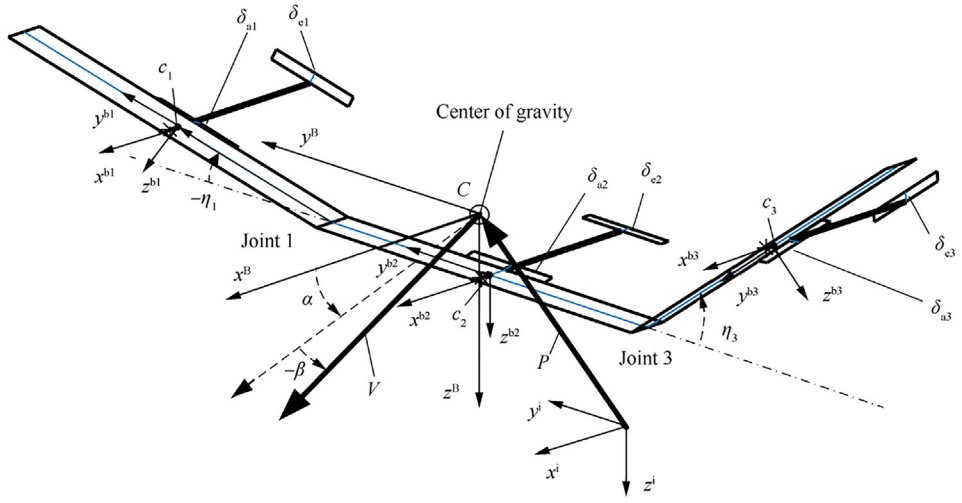

Fig. 1 Schematic diagram of configuration and frames.

2.1. Nonlinear flight dynamics of rigid motion

Equations of motion for HARW are comprised of translational dynamics of the center of gravity, and rotational dynamics about the center of gravity, which are given by

$$\begin{cases} m\boldsymbol{S}_V(V,\alpha,\beta)\dot{\boldsymbol{x}}_V = \boldsymbol{F}^{\mathrm{B}} - m\boldsymbol{\omega}\times\left[\boldsymbol{T}_{\mathrm{A}}^{\mathrm{B}}(\alpha,\beta)\boldsymbol{V}^{\mathrm{A}}\right] \\ \boldsymbol{I}_C^{\mathrm{B}}\dot{\boldsymbol{\omega}}^{\mathrm{B}} = \boldsymbol{M}^{\mathrm{B}} - \boldsymbol{\omega}^{\mathrm{B}}\times\left(\boldsymbol{I}_C^{\mathrm{B}}\boldsymbol{\omega}^{\mathrm{B}}\right) - \frac{\mathrm{d}}{\mathrm{d}t}\boldsymbol{I}_C^{\mathrm{B}}\boldsymbol{\omega}^{\mathrm{B}} \\ \dot{\boldsymbol{P}}^{i} = \boldsymbol{T}_{\mathrm{B}}^{i}(\phi,\theta,\psi)\boldsymbol{T}_{\mathrm{A}}^{\mathrm{B}}(\alpha,\beta)\boldsymbol{V}^{\mathrm{A}} \\ \dot{\boldsymbol{\Theta}} = \boldsymbol{S}_{\omega}(\phi,\theta)\boldsymbol{\omega}^{\mathrm{B}} \end{cases} \tag{1}$$

where, $\boldsymbol{\omega}^{\mathrm{B}} = [p, q, r]^{\mathrm{T}}$ is the vector form of angular velocity, where p, q, and r denote roll angle rate, pitch angle rate and yaw angle rate correspondingly. $\boldsymbol{\Theta} = [\phi, \theta, \psi]^{\mathrm{T}}$ denotes the array of attitude angles, where ϕ, θ, ψ are the roll angle, pitch angle and yaw angle. $\boldsymbol{V}^{\mathrm{A}} = [V,0,0]^{\mathrm{T}}$ denotes components of velocity in aerodynamic frame, $\boldsymbol{I}_C^{\mathrm{B}}$ is the inertial matrix about point C, $\boldsymbol{F}^{\mathrm{B}}$ and $\boldsymbol{M}^{\mathrm{B}}$ are force and moment components defined in body frame. $\boldsymbol{T}_{\mathrm{A}}^{\mathrm{B}}(\alpha,\beta)$ is the coordinate transformation matrix from aerodynamic frame to body frame, where α and β are the angle of attack and angle of sideslip. $\boldsymbol{T}_{\mathrm{B}}^{i}(\phi,\theta,\psi)$ is the coordinate transformation matrix from body frame to inertial frame. $\boldsymbol{S}_V(V, \alpha, \beta)$ and $\boldsymbol{S}_{\omega}(\phi, \theta)$ are state transition matrices of linear velocity and angle velocity, respectively.

2.2. Flexible dynamics of dihedral angles

Two additional degrees of freedom from structural dynamics of dihedral angles are integrated into the six-DOF rigid motion. The structural dynamics considered in this paper are restricted in the transverse plane. Equations of motion of the k-th dihedral angle are formulated as

$$\left(\boldsymbol{M}_{\mathrm{j},k}^{\mathrm{B}}\right)_x = \frac{\mathrm{d}}{\mathrm{d}t}\left(\boldsymbol{H}_{\mathrm{j},k}^{\mathrm{B}}\right)_x + \kappa_{\mathrm{c}}\dot{\eta}_{\mathrm{k}} + \kappa_{\mathrm{s}}\eta_k, k = 1,3 \tag{2}$$

where, $\boldsymbol{M}_{\mathrm{j},k}^{\mathrm{B}}$ is the moment from the k-th wing about the k-th joint, $\boldsymbol{H}_{\mathrm{j},k}^{\mathrm{B}}$ is the angular momentum of k-th wing about the k-th joint, $(*)_x$ denotes the x-component of a vector, κ_{c} and κ_{s} are damping coefficient and spring constant for the joint.

The local angular momentum about the k-th joint in the body frame is expressed as:

$$\boldsymbol{H}_{\mathrm{j},k}^{\mathrm{B}} = \boldsymbol{I}_{\mathrm{j},k}^{\mathrm{B}}\boldsymbol{\omega}_{\mathrm{j},k}^{\mathrm{B}} + m_k\left(\boldsymbol{r}_k^{\mathrm{B}}\right)\times\boldsymbol{V}_k^{\mathrm{B}} \tag{3}$$

where, $\boldsymbol{r}_k^{\mathrm{B}}$ are components of vector $\boldsymbol{r}_k$ in body frame, and the local angle velocity of the k-th wing $\boldsymbol{\omega}_{\mathrm{j},k}^{\mathrm{B}}$ is composed of the motion of rigid body $\boldsymbol{\omega}$ and the dynamics of joint $\dot{\eta}_k$, which is given by

$$\boldsymbol{\omega}_{\mathrm{j},k}^{\mathrm{B}} = \boldsymbol{\omega}^{\mathrm{B}} + [\dot{\eta}_k, 0, 0]^{\mathrm{T}} \tag{4}$$

The local velocity of the k-th wing is denoted as $\boldsymbol{V}_k$, components of which in body frame are obtained by

$$\boldsymbol{V}_k^{\mathrm{B}} = \boldsymbol{V}^{\mathrm{B}} + \frac{\mathrm{d}}{\mathrm{d}t}\left(-\boldsymbol{c}_k^{\mathrm{B}}\right) + \boldsymbol{\omega}^{\mathrm{B}}\times\left(-\boldsymbol{c}_k^{\mathrm{B}}\right) \tag{5}$$

where $\boldsymbol{c}_k^{\mathrm{B}}$ is the relative displacement from the CG of the k-th wing to the CG of the system in B-frame as shown in Fig. 2. Time derivation of the local angle momentum about the joint is obtained as.

$$\frac{\mathrm{d}}{\mathrm{d}t}\boldsymbol{H}_{\mathrm{j},k}^{\mathrm{B}} = \boldsymbol{I}_{\mathrm{j},k}^{\mathrm{B}}\dot{\boldsymbol{\omega}}_{\mathrm{j},k}^{\mathrm{B}} + \frac{\mathrm{d}}{\mathrm{d}t}\boldsymbol{I}_{\mathrm{j},k}^{\mathrm{B}}\boldsymbol{\omega}_{\mathrm{j},k}^{\mathrm{B}} + m_k\left(\boldsymbol{r}_k^{\mathrm{B}}\right)\times\dot{\boldsymbol{V}}_k^{\mathrm{B}} + m_k\left(\dot{\boldsymbol{r}}_k^{\mathrm{B}}\right)\times\boldsymbol{V}_k^{\mathrm{B}} \tag{6}$$

Substitute Eq. (6) to Eq. (2), the scaler form of structural equations of dihedral angles are formulated as.

$$\begin{cases} \boldsymbol{I}_{\mathrm{j}}\ddot{\eta}_1 = \left(\boldsymbol{M}_{\mathrm{j},1}^{\mathrm{B}}\right)_x - \left[\kappa_c - \frac{m_1 s}{2}(v\cos\eta_1 + w\sin\eta_1)\right]\dot{\eta}_1 \\ \qquad -\kappa_s\eta_1 - \frac{m_1 s}{2}(\dot{v}_1\sin\eta_1 - \dot{w}_1\cos\eta_1) - \boldsymbol{I}_{\mathrm{j}}\dot{p} \\ \boldsymbol{I}_{\mathrm{j}}\ddot{\eta}_3 = \left(\boldsymbol{M}_{\mathrm{j},3}^{\mathrm{B}}\right)_x - \left[\kappa_c + \frac{m_3 s}{2}(v\cos\eta_3 + w\sin\eta_3)\right]\dot{\eta}_3 \\ \qquad -\kappa_s\eta_3 - \frac{m_3 s}{2}(\dot{v}_3\sin\eta_3 - \dot{w}_3\cos\eta_3) - \boldsymbol{I}_{\mathrm{j}}\dot{p} \end{cases} \tag{7}$$

where $\boldsymbol{I}_{\mathrm{j}} = \boldsymbol{I}_x^{\mathrm{b}} + ms^2/4$.

2.3. Mass and inertial matrix

Assume that the mass of bilateral wings is the same $\tilde{m} = m_1 = m_3$, and the mass of elevators is negligible. The mass of central wing is integrated with the load mass and expressed as $m_2 = k_m\tilde{m}$, $(k_m \geq 1)$. The inertial tensor of

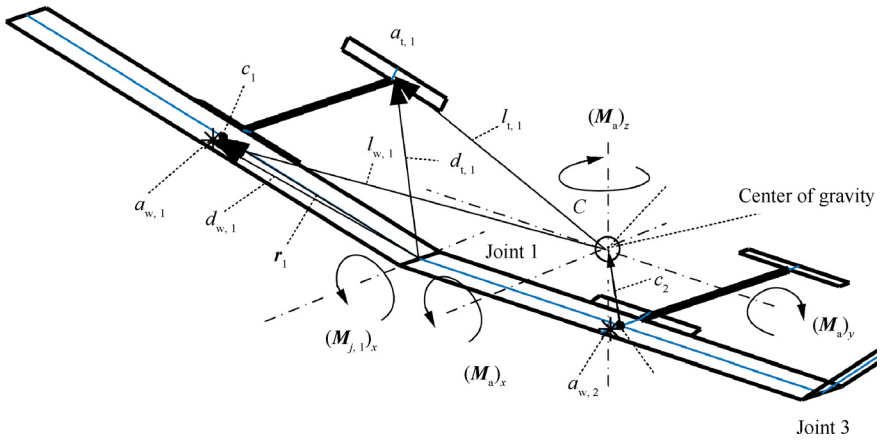

Fig. 2 Illustration of applied moments.

the k-th wing is defined as $\boldsymbol{I}_{c,k}$, which can be represented in different frames:

$$\boldsymbol{I}_{c,k} = \left(\boldsymbol{e}^{\mathrm{b}k}\right)^{\mathrm{T}} \boldsymbol{I}_{c,k}^{\mathrm{b}k} \boldsymbol{e}^{\mathrm{b}k} = \left(\boldsymbol{e}^{\mathrm{B}}\right)^{\mathrm{T}} \boldsymbol{I}_{c,k}^{\mathrm{B}} \boldsymbol{e}^{\mathrm{B}} \tag{8}$$

where, $\boldsymbol{e}^{\mathrm{b}k}$ are the base vectors of the local body frame, $\boldsymbol{e}^{\mathrm{B}}$ are the base vectors of the body frame, $\boldsymbol{I}_{c,k}^{\mathrm{b}k}$ is the inertial matrix in local body frame, $\boldsymbol{I}_{c,k}^{\mathrm{B}} = \boldsymbol{T}_{\mathrm{b}k}^{\mathrm{B}} \boldsymbol{I}_{c,k}^{\mathrm{b}k} \boldsymbol{T}_{\mathrm{B}}^{\mathrm{b}k}$ is the inertial matrix in body frame, and $\boldsymbol{T}_{\mathrm{b}k}^{\mathrm{B}}$ is the coordinate transformation matrix from local body frame to body frame.

The inertial matrix of the k-th wing about C in B-frame is then calculated as

$$\boldsymbol{I}_{C,k}^{\mathrm{B}} = \boldsymbol{I}_{c,k}^{\mathrm{B}} + m_k \left[\langle \boldsymbol{c}_k^{\mathrm{B}}, \boldsymbol{c}_k^{\mathrm{B}} \rangle \boldsymbol{I} - \boldsymbol{c}_k^{\mathrm{B}} \otimes \boldsymbol{c}_k^{\mathrm{B}} \right] \tag{9}$$

where, $\boldsymbol{I}$ is the identity matrix, $<\cdot>$ is the inner product, $\otimes$ is the Kronecker product, and $\boldsymbol{c}_k^{\mathrm{B}}$ is components of vector $\boldsymbol{c}_k$ in body frame. The inertial matrix about center of gravity C of HARW in body frame is expressed as

$$\boldsymbol{I}_C^{\mathrm{B}}(k_m, \eta_1, \eta_3) = \sum_{k=1}^{3} \boldsymbol{I}_{C,k}^{\mathrm{B}} \tag{10}$$

The quasi-steady assumption of inertia properties is invalid when considering the structure dynamics of dihedral angles. The time derivative of the inertial matrix is dominated by the dynamic of dihedral angles and represented as

$$\frac{\mathrm{d}}{\mathrm{d}t} \boldsymbol{I}_C^{\mathrm{B}} = \frac{\partial}{\partial \eta_1} \boldsymbol{I}_C^{\mathrm{B}}(k_m, \eta_1, \eta_3) \dot{\eta}_1 + \frac{\partial}{\partial \eta_3} \boldsymbol{I}_C^{\mathrm{B}}(k_m, \eta_1, \eta_3) \dot{\eta}_3 \tag{11}$$

2.4. Forces and moments

The force acting on the HARW is composed of gravitational force $\boldsymbol{F}_{\mathrm{g}}$, propulsive force $\boldsymbol{F}_T$, and aerodynamic force $\boldsymbol{F}_{\mathrm{a}}$, whereas the moment is composed of propulsive moment $\boldsymbol{M}_T$ and aerodynamic moment $\boldsymbol{M}_{\mathrm{a}}$. The total force and moment acting on the HARW defined in the body frame are calculated as

$$\begin{cases} \boldsymbol{F}^{\mathrm{B}} = \boldsymbol{F}_{\mathrm{a}}^{\mathrm{B}} + \boldsymbol{F}_T^{\mathrm{B}} + \boldsymbol{F}_{\mathrm{g}}^{\mathrm{B}} \\ \boldsymbol{M}^{\mathrm{B}} = \boldsymbol{M}_{\mathrm{a}}^{\mathrm{B}} + \boldsymbol{M}_T^{\mathrm{B}} \end{cases} \tag{12}$$

Besides, the hinge moment about the joint in body frame is calculated by

$$\boldsymbol{M}_{\mathrm{j},k}^{\mathrm{B}} = \boldsymbol{r}_k^{\mathrm{B}} \times \left(\boldsymbol{F}_{\mathrm{g},k}^{\mathrm{B}} + \boldsymbol{F}_{\mathrm{a},k}^{\mathrm{B}} \right) \tag{13}$$

where $\boldsymbol{r}_k^{\mathrm{B}}$, $\boldsymbol{F}_{\mathrm{g},k}^{\mathrm{B}}$ and $\boldsymbol{F}_{\mathrm{a},k}^{\mathrm{B}}$ are components in body frame of the gravitational force and aerodynamic force of the k-th wing. The schematic illustration for definition of moments is shown in Fig. 2.

Let T_i, i = 1,2,3 be the thrust provided by each propeller. The symmetrical thrust strategy is adopted for the longitudinal channel, whereas the antisymmetrical thrust strategy is for the lateral channel. Let T_{d} denotes the deviation of thrust, and we assume that $T_3 = T_2 + T_{\mathrm{d}}$, $T_1 = T_2 - T_{\mathrm{d}}$. Therefore, components of thrust in the body frame are expressed as $\boldsymbol{F}_T^{\mathrm{B}} = 3[\,T_2 \quad 0 \quad 0\,]^{\mathrm{T}}$.

The moment provided by propellers is given by.

$$\begin{aligned} \boldsymbol{M}_T^{\mathrm{B}} = \sum_{k=1}^{3} -\boldsymbol{c}_k^{\mathrm{B}} \times \boldsymbol{T}_k^{\mathrm{B}} = & \begin{bmatrix} 0 \\ \sin\eta_1 - \sin\eta_3 \\ -\cos\eta_1 + \cos\eta_3 \end{bmatrix} \frac{s(k_m - 1)}{2(2 + k_m)} T_2 \\ & + \begin{bmatrix} 0 \\ -\sin\eta_1 - \sin\eta_3 \\ 2 + \cos\eta_1 + \cos\eta_3 \end{bmatrix} \frac{s}{2} T_{\mathrm{d}} \end{aligned} \tag{14}$$

If the mass of the centre-wing equals the mass of the side-wing, that is k = 1, then the thrust provided by the central propeller will not generate any moment. Otherwise, T_2 will generate an additional moment due to asymmetrical deformation.

The aerodynamic forces are calculated in the local aerodynamic frame. Forces defined with respect to the center of gravity of the vehicle in the wind axis frame are denoted.

$$\boldsymbol{F}_{\mathrm{a}}^{\mathrm{B}} = \boldsymbol{F}_{\mathrm{w}}^{\mathrm{B}} + \boldsymbol{F}_{\mathrm{t}}^{\mathrm{B}} \tag{15}$$

where, $\boldsymbol{F}_{\mathrm{w}}^{\mathrm{B}}$ and $\boldsymbol{F}_{\mathrm{t}}^{\mathrm{B}}$ are the driven force from the three wing sections and the three tail sections respectively.

Given that the aerodynamic forces are driven by the local angle of attack, the velocity is transformed into the local body frame.

$$V_k^{bk} = \boldsymbol{T}_{\mathrm{B}}^{bk}(\eta_k)\boldsymbol{V}_k^{\mathrm{B}} = \left[u_k^{\mathrm{b}}, v_k^{\mathrm{b}}, w_k^{\mathrm{b}}\right]^{\mathrm{T}} \tag{16}$$

The side force for straight wings in subsonic flight is assumed to be zero. Besides, there are no vertical fins and rudders. Therefore, the local pressure-driven forces defined in the local aerodynamic frame are expressed as

$$\boldsymbol{F}_{\mathrm{w},k}^{ak} = \begin{bmatrix} -D_{\mathrm{w},k} \\ 0 \\ -L_{\mathrm{w},k} \end{bmatrix}, \boldsymbol{F}_{\mathrm{t},k}^{ak} = \begin{bmatrix} -D_{\mathrm{t},k} \\ 0 \\ -L_{\mathrm{t},k} \end{bmatrix}, k = 1,2,3 \tag{17}$$

where, the local lift and drag on the wing and tail sections are defined as

$$\begin{cases} L_{\mathrm{w},k} = \bar{q}_i S_{\mathrm{w}} C_{L\mathrm{w},k}, C_{L\mathrm{w},k} = C_{L,\alpha}\alpha_k + C_{L,\delta}\delta_{\mathrm{a},k} \\ L_{\mathrm{t},k} = \bar{q}_i S_{\mathrm{t}} C_{L\mathrm{t},k}, C_{L\mathrm{t},k} = C_{L,\alpha}(\alpha_k + \delta_{\mathrm{e},k}) \\ D_{\mathrm{w},k} = \bar{q}_i S_{\mathrm{w}} C_{D\mathrm{w},k}, C_{D\mathrm{w},k} = C_{D,0} + \kappa_D C_{L\mathrm{w},k}^2 \\ D_{\mathrm{t},k} = \bar{q}_i S_{\mathrm{t}} C_{D\mathrm{t},k}, C_{D\mathrm{t},k} = C_{D,0} + \kappa_D C_{L\mathrm{t},k}^2 \end{cases} \tag{18}$$

where, $\bar{q}_i$ is the local dynamic pressure, $\delta_{\mathrm{a},k}$ is the aileron deflection angle, and $\delta_{\mathrm{e},k}$ is the elevator deflection angle for k = 1,2,3.

The aerodynamic moment on HARW is expressed as.

$$\boldsymbol{M}_{\mathrm{a}}^{\mathrm{B}} = \sum_{k=1}^{3}\left[\boldsymbol{T}_{\mathrm{b}k}^{\mathrm{B}}(\eta_k)\boldsymbol{M}_k^{\mathrm{b}} + \boldsymbol{l}_{\mathrm{w},k}^{\mathrm{B}} \times \boldsymbol{F}_{\mathrm{w},k}^{\mathrm{B}} + \boldsymbol{l}_{\mathrm{t},k}^{\mathrm{B}} \times \boldsymbol{F}_{\mathrm{t},k}^{\mathrm{B}}\right] \tag{19}$$

where, $\boldsymbol{l}_{\mathrm{w},k}^{\mathrm{B}}$ and $\boldsymbol{l}_{\mathrm{t},k}^{\mathrm{B}}$ denote the components of the vectors that point form C to the quarter cord of the wing and the tail, respectively (see Fig. 2).

The roll moment and yaw moment in the local body frame are neglected due to the flat wing assumption. Hence, the aerodynamic moment defined in the local body frame is expressed as.

$$\boldsymbol{M}_k^{\mathrm{b}} = [0, M_k, 0]^{\mathrm{T}} \tag{20}$$

where, the pitch moment is calculated by.

$$M_k = q_k c_{\mathrm{w}} S_{\mathrm{w}} C_{m,k}, C_{m,k} = C_{m,0} + C_{m,\delta}\delta_{\mathrm{a},k} \tag{21}$$

where c_{w} is the cord length of the wing.

Finally, the hinge moment at the j-th joint is defined as.

$$\boldsymbol{M}_{\mathrm{j},k}^{\mathrm{B}} = \boldsymbol{r}_k^{\mathrm{B}} \times \boldsymbol{F}_{\mathrm{g},k}^{\mathrm{B}} + \boldsymbol{d}_{\mathrm{w},k}^{\mathrm{B}} \times \boldsymbol{F}_{\mathrm{w},k}^{\mathrm{B}} + \boldsymbol{d}_{\mathrm{t},k}^{\mathrm{B}} \times \boldsymbol{F}_{\mathrm{t},k}^{\mathrm{B}} \tag{22}$$

where, $\boldsymbol{d}_{\mathrm{w},k}^{\mathrm{B}}$ and $\boldsymbol{d}_{\mathrm{t},k}^{\mathrm{B}}$ are components of the displacement from the joint to the center of pressure of wing and tail, respectively (see Fig. 2). The x-components of hinge moment at joints are given by.

$$\begin{cases} \left(\boldsymbol{M}_{\mathrm{j},1}^{\mathrm{B}}\right)_x = \frac{s}{2}\left[\left(\boldsymbol{F}_{\mathrm{w},1}^{\mathrm{B}}\right)_z + \left(\boldsymbol{F}_{\mathrm{t},1}^{\mathrm{B}}\right)_z + m_1 g\cos\theta\cos\phi\right] \\ \cdot\cos\eta_1 - \frac{s}{2}\left[\left(\boldsymbol{F}_{\mathrm{w},1}^{\mathrm{B}}\right)_y + \left(\boldsymbol{F}_{\mathrm{t},1}^{\mathrm{B}}\right)_y + m_1 g\cos\theta\sin\phi\right]\sin\eta_1 \\ \left(\boldsymbol{M}_{\mathrm{j},3}^{\mathrm{B}}\right)_x = -\frac{s}{2}\left[\left(\boldsymbol{F}_{\mathrm{w},3}^{\mathrm{B}}\right)_z + \left(\boldsymbol{F}_{\mathrm{t},3}^{\mathrm{B}}\right)_z + m_3 g\cos\theta\cos\phi\right] \\ \cdot\cos\eta_3 + \frac{s}{2}\left[\left(\boldsymbol{F}_{\mathrm{w},3}^{\mathrm{B}}\right)_y + \left(\boldsymbol{F}_{\mathrm{t},3}^{\mathrm{B}}\right)_y + m_3 g\cos\theta\sin\phi\right]\sin\eta_3 \end{cases} \tag{23}$$

The coupling of flight dynamics is reflected in two aspects. First, the attitude dynamics Eq. (1) is coupled with flexible mode via the varying inertia properties. Second, the nonlinear flight dynamics of HARW consist of nonlinear flight dynamics of rigid motion and flight dynamics of dihedral angles.

Fig. 3 shows the framework for the nonlinear coupled flight dynamics of HARW. The thrust, aerodynamic, and inertia are related to flexible states η and $\dot{\eta}$; whereas, the flexible equations are affected by rigid body state V, α, β and $\dot{p}$. Coupled nonlinear aeroelasticity of HARW is complicated and contains many states, making it unsuitable for control synthesis. Hence, a reduced model for the control system becomes quite essential.

3. Nonlinear coupled flight dynamics

The preceding section provides the modelling issues for HARW. Next, three linearized models at the trim condition with different loads are considered, namely HARW with an empty load, half load, and full load, to reveal the complex

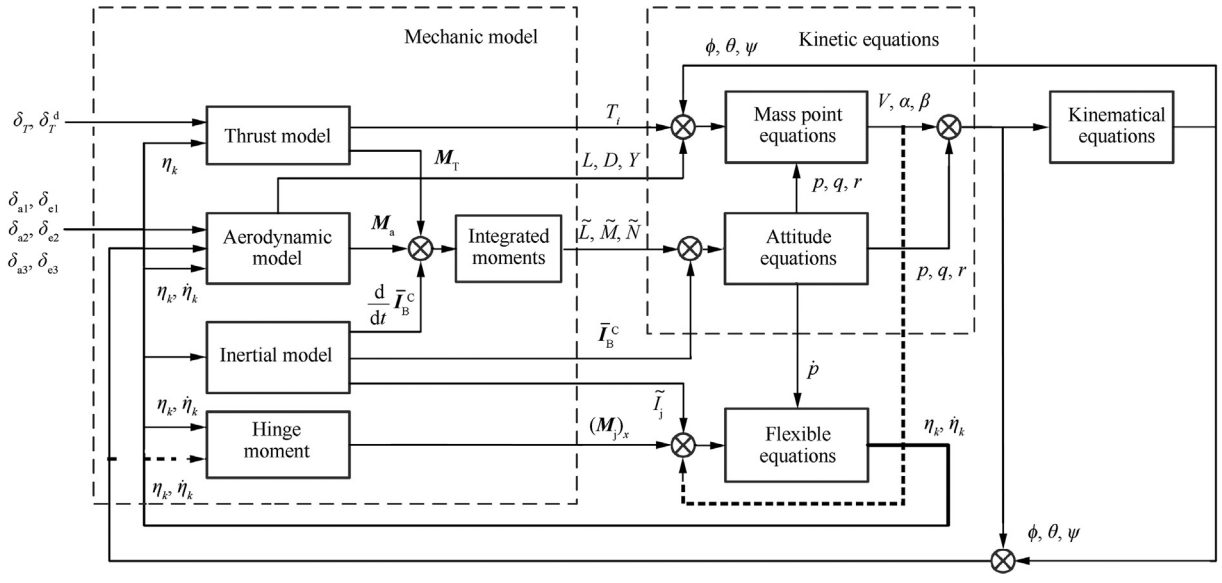

Fig. 3 Framework for the nonlinear coupled flight dynamics of HARW.

interaction between rigid body dynamics and flexible dynamics. The results are given by modal sensitivity and Relative Gain Array (RGA) analysis.

3.1. Input/output selection based on RGA

The pairing of inputs and outputs affects the performance, complexity, and costs of the control system. Generally, the condition number and the RGA are measures to quantify the degree of directionality and the level of interactions in MIMO systems. The RGA of a transfer matrix, defined in the frequency domain, is a simple and effective screening approach for selecting inputs and outputs to avoid the combinatorial problem and a good indicator of sensitivity to uncertainty in the input channels. Compared with the condition number, the primary advantage of RGA is scaling independence on inputs and outputs.

The RGA of a non-singular square transfer function matrix $\boldsymbol{G}$ (jω) is defined as

$$\boldsymbol{\Lambda}_G(\mathrm{j}\omega) = \boldsymbol{G}(\mathrm{j}\omega) \odot \boldsymbol{G}(\mathrm{j}\omega)^{-\mathrm{T}} \tag{24}$$

where $\odot$ is the Hadamard product of matrices. The sum-norm of RGA is very close to the minimized condition number, which indicates that plants with large RGA elements are always ill-conditioned. The definition of the RGA may be generalized to non-square matrices by using the pseudo inverse to identify the extra inputs and outputs.

Theorem (RGA and input–output projections)[33]: The i-th row sum of the RGA is equal to the square of the i-th output projection, and the j-th column sum of the RGA is equal to the square of the j-th input projection.

$$\begin{cases} \sum_{j=1}^{m} \lambda_{ij} = \|\boldsymbol{e}_i^{\mathrm{T}} \boldsymbol{U}_{\mathrm{r}}\|_2^2 \\ \sum_{i=1}^{l} \lambda_{ij} = \|\boldsymbol{e}_j^{\mathrm{T}} \boldsymbol{V}_{\mathrm{r}}\|_2^2 \end{cases} \tag{25}$$

where, $\boldsymbol{U}_{\mathrm{r}}$ and $\boldsymbol{V}_{\mathrm{r}}$ are the matrices of singular value decomposition of $\boldsymbol{G} = \boldsymbol{U}_{\mathrm{r}}\Sigma_{\mathrm{r}}\boldsymbol{V}_{\mathrm{r}}^{\mathrm{H}}$.

The theorem provides a practical approach to screening invalid input for interested/selected output. For decentralized control, we prefer the pairing of inputs and output where the RGA number at crossover frequencies is close to 0.

3.2. Flight control structure

This paper selects the control outputs as V, θ in the longitudinal channel and β, ϕ in the lateral/directional channel. Moreover, we consider the flexibility to reveal the coupling of flight and structural dynamics. Hence, there are two extra inputs in the flight control of HARW.

The pairing of inputs and outputs is challenging to identify since there are no dominant elements and few negligible elements in the column sum of the RGA-matrix, as shown in Table 1. Therefore, we modify the inputs by combining flap deflections from physical insight with the following expression.

$$\begin{cases} \delta_{\mathrm{e}}^{\mathrm{s}} = \frac{1}{3}\sum_{i=1}^{3}\delta_{\mathrm{e}i} & \delta_{\mathrm{ac}} = \delta_{\mathrm{a2}} \\ \delta_{\mathrm{e}}^{\mathrm{as}} = \frac{1}{2}(\delta_{\mathrm{e3}} - \delta_{\mathrm{e1}}) & \delta_{\mathrm{a1}}^{\mathrm{d}} = \delta_{\mathrm{a1}} - \delta_{\mathrm{a2}} \\ \delta_{\mathrm{e}}^{\mathrm{d}} = \delta_{\mathrm{e2}} - (\delta_{\mathrm{e1}} + \delta_{\mathrm{e3}}) & \delta_{\mathrm{a3}}^{\mathrm{d}} = \delta_{\mathrm{a3}} - \delta_{\mathrm{a2}} \end{cases} \tag{26}$$

where, $\delta_{\mathrm{e}}^{\mathrm{s}}$ denotes the symmetrical deflection of all three elevators, $\delta_{\mathrm{e}}^{\mathrm{as}}$ denotes the asymmetrical deflection of bilateral elevators, $\delta_{\mathrm{e}}^{\mathrm{d}}$ denotes the difference deflection between central elevator and bilateral elevators, δ_{ac} denotes the deflection of central aileron, $\delta_{\mathrm{a1}}^{\mathrm{d}}$ denotes the difference deflection between 1-st aileron and central aileron, $\delta_{\mathrm{a3}}^{\mathrm{d}}$ denotes the difference deflection between 3-rd aileron and central aileron. Illustration of the modified control inputs is presented in Fig. 4.

The column sums of RGA-matrix with all candidate modified inputs are listed in Table 2. The dominated elements are highlighted in bold. Items with zero-sum for the output are assumed not to affect the output, which is negligible. For example, $\delta_{\mathrm{e}}^{\mathrm{s}}$ input plays an important role in V & θ; on the other hand, $\delta_{\mathrm{e}}^{\mathrm{as}}$ and δ_{T}^{d} have no effect in V & θ, but other non-zero items cannot be neglected by only using RGA-matrix.

Table 3 lists the maximum RGA-number of MIMO with specified outputs at a steady state. The result shows that the interaction of velocity control and FPA control recedes with more extensive deformation, whereas lateral/directional control interaction intensifies. For output V & θ, the RGA number of both δ_T & $\delta_{\mathrm{e}}^{\mathrm{s}}$ and δ_T & $\delta_{\mathrm{a}}^{\mathrm{c}}$ are almost the same, so the frequency domain characteristics is analyzed to determine the pairing.

Plants with significant RGA elements around the crossover frequency are fundamentally difficult to control.[34] Significant RGA elements mean even a tiny difference in the control input can lead to a big difference in the output. In particular, plants with significant RGA elements cannot utilize decouplers or other inverse-based controllers. Inputs corresponding to col-

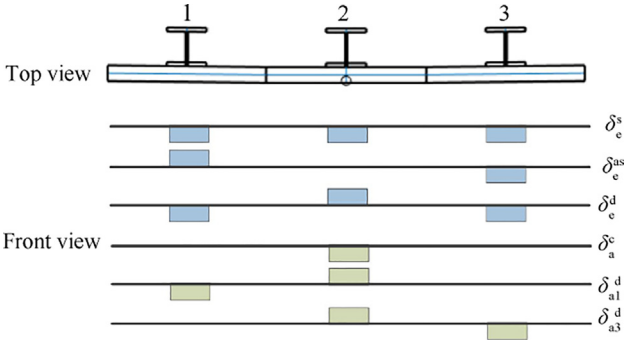

Fig. 4 Illustration of modified control inputs.

Table 1 Column sum of elements in RGA-matrix with physical inputs.

Outputs	δ_{a2}	δ_{e2}	δ_{a1}	δ_{e1}	δ_{a3}	δ_{e3}	δ_T	$\delta^{\mathrm{d}}{}_T$
V & θ	0.34	0.38	0.25	0.33	0.25	0.33	0.11	0
β & ϕ	0	0	0.46	0.23	0.46	0.23	0	0.62
η & $\dot{\eta}$	0.56	0.06	0.60	0.05	0.60	0.05	0	0.08

Table 2 Column sum of elements in RGA-matrix with modified inputs.

Outputs	δ_{a2}	δ_{e2}	δ_{a1}	δ_{e1}	δ_{a3}	δ_{e3}	δ_T	$\delta^d{}_T$
V & θ	1.00	0	0.01	0.80	0.08	0.08	0.03	0
β & ϕ	0	0.63	0	0	0.44	0.44	0	0.48
η & $\dot{\eta}$	0.01	0.04	0.14	0	0.87	0.87	0	0.08

Table 3 Maximum RGA-number with different pairing of inputs and outputs.

Outputs	Inputs	Maximum RGA-number (dB)		
		No load	Half load	Full load
V & θ	δ_T & δ_e^s	249.6	52.8	5.8
	δ_a^c & δ_e^s	3903.7	674.9	18.2
	δ_T & δ_a^c	247.1	51.2	5.3
β & ϕ	δ_T^d & δ_e^{as}	16.2	30.9	143.4
η_1&η_3	δ_{a1}^d & δ_{a3}^d	57.2	27.9	10.1

umns in RGA where the sum of the elements is much smaller than one can be negligible.

Furthermore, the RGA-number provides a measure of two-way interaction for the square MIMO, which is the sum-norm of the difference between the RGA-matrix and the identity matrix.

$$\gamma_{\mathrm{RGA}} = \| \Lambda(\boldsymbol{G}) - \boldsymbol{I} \|_{\mathrm{sum}} \tag{27}$$

The RGA characteristics of HARW with full load are shown in Fig. 5. It is better to choose δ_T & δ_e^s as control input for V & θ, because the maximum RGA-number and RGA-element are lower for the most frequency.

It should be noted that to realize the control of the structure, the HARW needs more control surfaces than the conventional aircraft. For the model in this paper, after RGA-number and RGA-element analysis, a reasonable way is to control the rolling with the differential elevator on both sides and the structure with ailerons. The ailerons of conventional aircraft are often used to control roll and sideslip. For the structure control of large flexible aircraft, piezoelectric materials are proposed in the literature, which is a promising approach.

Fig. 6 shows the frequency-varying diagonal element in RGA for lateral and flexible channels. RGA-element in the lateral channel is greater than 10, implying that the inverse-based controller is not robust to diagonal input uncertainty. Besides, the inverse polarity of the diagonal element within the frequency of interest indicates an RHP-zero.

3.3. Formulation of COM

The control-oriented model for HARW comprises two parts: simplification of flight dynamics and formulation of the analytical form of the mechanical model. The first part is generally divided into longitudinal and lateral dynamics with uniform formulations based on reasonable assumptions. However, the second part is closely related to the subject of interest. Hence, in this section, we focus on the formulation of the mechanical property of HARW with the Curve-Fitting Model (CFM). The

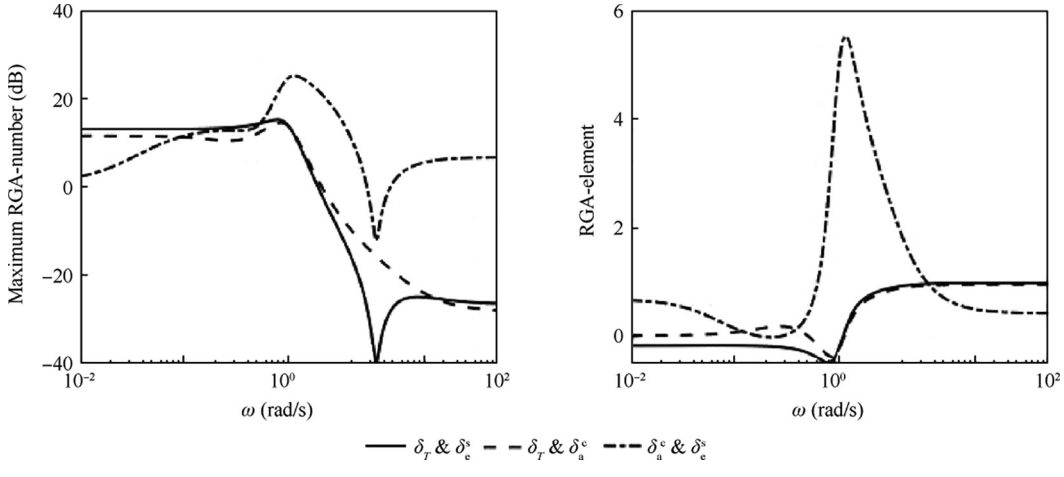

Fig. 5 RGA characteristics of HARW with full loads.

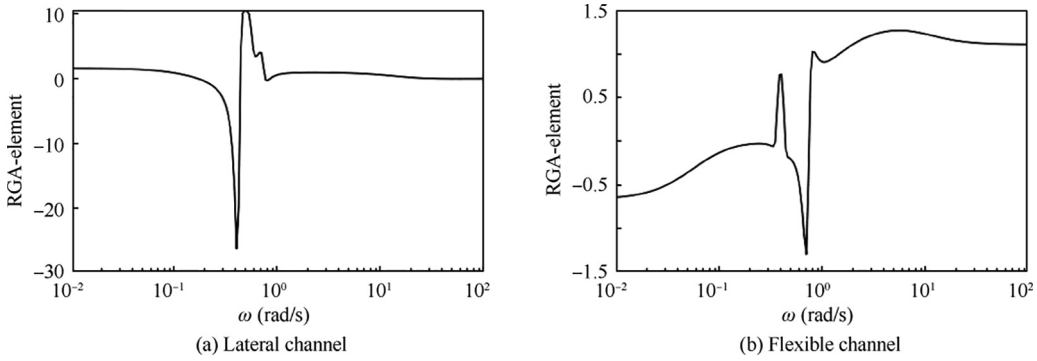

Fig. 6 Diagonal element in RGA-matrix.

central mass drives the deformation of HARW. We assume that the mass of the central node remains constant. Therefore, two CFM are formulated for HARW with empty and full loads to investigate the coupled flight dynamics.

Two principles are considered in the formulation of CFM. First, the prediction of CFM is allowed to have numerical inaccuracy but has to ensure polarity robustness. Second, terms in CFM prefer simplification with physical significance rather than complicated forms. Hereto, we present the formulation of mechanical CFM, including aerodynamic force coefficient, aerodynamic moment coefficient, and hinge moment coefficient, as follows.

The aerodynamic force coefficients are formulated as.

$$\begin{cases} C_L = C_L^0 + C_L^\alpha \alpha + C_L^{\dot{\eta}_s}\dot{\eta}_s + C_L^{\delta_e^s}\delta_e^s + C_L^{\delta_a^c}\delta_a^c + C_L^{\delta_a^d}\left(\delta_{a1}^d + \delta_{a3}^d\right) \\ C_D = C_D^0 + \kappa_D C_L^2 + C_D^{\dot{\eta}_{as}p}\dot{\eta}_{as}p + C_D^{p^2}p^2 \\ C_Y = C_Y^\beta \beta + C_Y^{\eta_{as}}\eta_{as} + C_Y^{p\eta_s}p\eta_s + C_Y^{\eta_s\dot{\eta}_{as}}\eta_s\dot{\eta}_{as} + C_Y^{\delta_a^d}\left(\delta_{a3}^d - \delta_{a1}^d\right) + C_Y^{\delta_e^{as}}\delta_e^{as} \end{cases} \tag{28}$$

where, $\eta_s = \eta_3 - \eta_1$ and $\eta_{as} = \eta_3 - \eta_1$ represent the symmetry and asymmetry change of structural dihedral angle, respectively.

The aerodynamic moment coefficients are formulated as.

$$\begin{cases} C_l = C_l^\beta \beta + C_l^p p + C_l^{\dot{\eta}_{as}}\dot{\eta}_{as} + C_l^{\delta_e^{as}}\delta_e^{as} + C_l^{\delta_a^d}\left(\delta_{a3}^d - \delta_{a1}^d\right) \\ C_m = C_m^0 + C_m^\alpha \alpha + C_m^{\dot{\eta}_s}\dot{\eta}_s + C_m^{\delta_e^s}\delta_e^s + C_m^{\delta_a^c}\delta_a^c + C_m^{\delta_a^d}\left(\delta_{a1}^d + \delta_{a3}^d\right) \\ C_n = C_n^\beta \beta + \left(C_n^{\alpha p}p + C_n^{\alpha\dot{\eta}_{as}}\dot{\eta}_{as}\right)\alpha + C_n^r r + C_n^{\alpha\delta_e^{as}}\alpha\delta_e^{as} \end{cases} \tag{29}$$

The hinge moment coefficients are formulated as.

$$\begin{aligned} C_{hi} = {} & C_{hi}^0 + C_{hi}^\alpha \alpha + C_{hi}^\beta \beta + C_{hi}^p p + C_{hi}^{\dot{\eta}_i}\dot{\eta}_i + C_{hi}^{\delta_a^c}\delta_a^c + C_{hi}^{\delta_{ai}^d}\delta_{ai}^d \\ & + C_{hi}^{\delta_e^{as}}\delta_e^{as} + C_{hi}^{\delta_e^d}\delta_e^d + C_{hi}^{\delta_e^s}\delta_e^s \end{aligned} \tag{30}$$

All coefficients in these CFM are presented in the Appendix A for HARW with Empty Load (EL) and Full Load (FL).

4. Numerical simulations

4.1. Trim characteristics analysis

To verify the results, we refer to the early research results in Ref. 34, and compare the trimmed character and dynamic stability. The trim analysis is carried out to illustrate that the reduced HARW model can capture the typical flight dynamics characteristic observed in the higher fidelity models. Fig. 7 shows the structural deformation and the flight angle of attack as a function of the aircraft's payload weight, where the red dotted line represents the reference value in Ref. 34. The additional load at the centre makes the deformation significant, leading to a decrease in the effective lift area but a significant lift to balance the weight. As a result, the trim angle of attack increases. The simulated results in this paper are consistent with those in the literature, both numerically and regularly.

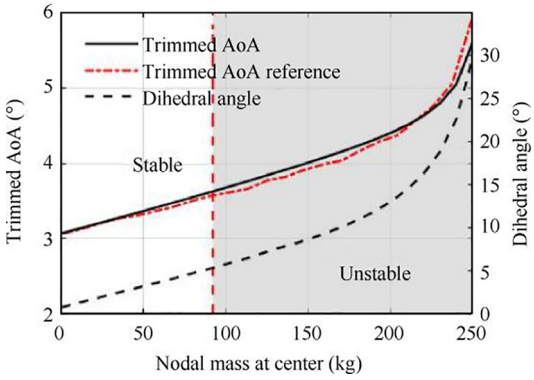

Fig. 7 Trimmed AoA and dihedral angle with nodal mass at center.

Fig. 8 illustrates the variation of modal frequencies ω_n and damping ratios ζ as the deformed dihedral angle goes large. Unstable phugoid mode with large deformation is observed in the simulation, which is consistent with published research. Besides, the frequency of the phugoid mode increases while the damping decreases as the deformation goes large. The short-period mode shows a drastic change in HARW. The root rushes with added deformation, and the pair of complex-conjugate short-period roots merge to become two real roots. The HARW does not show a classical short-period mode in its deformed state when loaded sufficiently.

The variation of the lateral modes is mainly reflected in the modal frequencies. However, the stability of DRM decreases at large deformation. The frequency of FOM increases and decreases with dihedral increasing, and the damping increases simultaneously. The FDM presents overdamping phenomenon. However, one of the eigenvalues becomes closer to

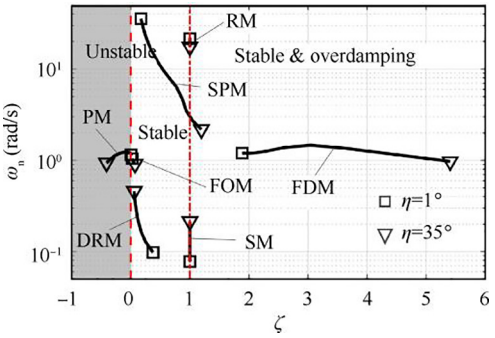

Fig. 8 Variation of modal frequencies and damping ratios with aggravation of deformation.

the imaginary axis with dihedral increasing, which means a prolonged decay in the response of HARW of large deformation.

4.2. Open-loop simulations

Lateral and structural responses are mainly analyzed in this section. The case studies are presented at full, half, and empty loads. Case 1 is excited with an antisymmetric initial dihedral disturbance to generate both longitudinal and lateral motion, where there is a 2° deviation for η_1 and a 4° deviation for η_3. Case 2 is excited with an asymmetric step elevator input for lateral motion.

4.2.1. Disturbance of asymmetric deformation

For Case 1, Fig. 9 shows the variation of states in 20 s. For the exact structure perturbation, the smaller the load, the larger the response amplitude of the transverse and lateral states. On the contrary, the amplitude of longitudinal state response increases. That is to say, the load increase will increase the lateral inertia and decrease the longitudinal inertia. The longitudinal dynamics diverge around 15 s with full loads. The sideslip angle mainly manifests as the DRM, and the frequency increases with the deformation. The structure and lateral motion coupling are mainly manifested in yaw angular rate. The results of response analysis are consistent with those of modal analysis. The difference in dihedral angle motion grows as load increases. The system goes from stable to divergent at the same time. It can be speculated that a significant difference in structure motion aggravates the divergence of the system. Asymmetric movement of the structure leads to lateral movement of the HARW, which requires asymmetric deflection of the rudder surface for control.

4.2.2. Differential deflection of elevators

Case 2 addresses the asymmetric loading. Results for this case are shown in Fig. 10. The differential elevator input influences little on the longitudinal motion even at the beginning of the full loads case, consistent with previous input–output pairing results. The frequency of sideslip oscillation increases with the increase of deformation, the yaw angular rate attenuates slowly, and the angular roll rate is affected by elastic motion and exhibits oscillation and damping characteristics simultaneously. The time-domain response verifies the modal analysis

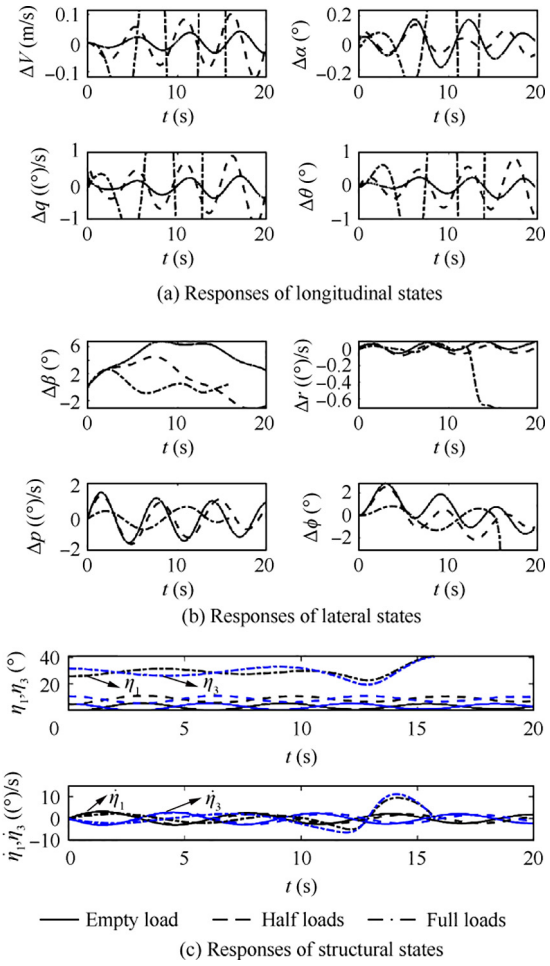

Fig. 9 Responses on structural asymmetric disturbance.

results. Besides, the displacement response with a full load in the y-direction is opposite with empty and half load case, indicating that the deformation strongly influences the effect of control input.

To show the flight process more intuitively, we present the 3D simulation of nonlinear dynamics of HARW with static stability and unstable cases in Fig. 11.

4.3. Close-loop simulations

The control inputs are thrust, centre elevator, and outer elevators, while the other control surfaces are fixed at trim. The goal is to stabilize the system to trim perturbations in dihedral angles in the initial condition. The LQG (Linear-Quadratic-Gaussian) regulator is used for controller design. First of all, the control-oriented model is linearized at the trim point. Then, the linearized model is decoupled from the longitudinal, lateral and flexible motion.

The LQG method minimizes the cost function with statistical assumption of input and output disturbances.

$$\begin{cases} \dot{\boldsymbol{x}} = \boldsymbol{A}\boldsymbol{x} + \boldsymbol{B}\boldsymbol{u} + \boldsymbol{w} \\ \boldsymbol{y} = \boldsymbol{C}\boldsymbol{x} + \boldsymbol{v} \end{cases} \tag{31}$$

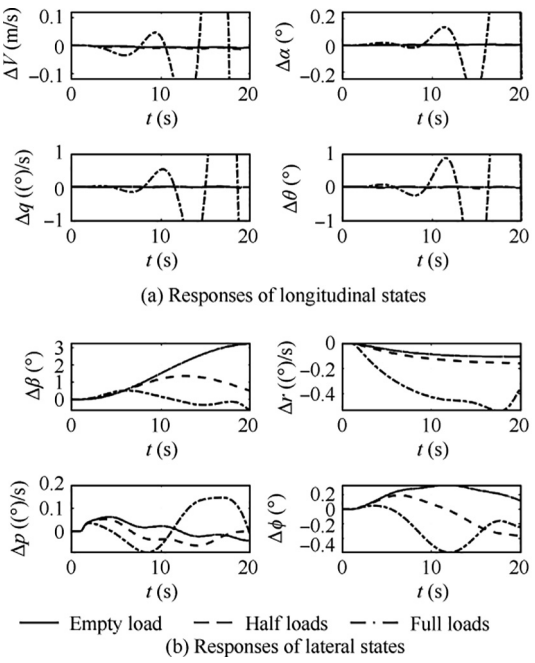

Fig. 10 Responses on differential deflection of elevators with different loads.

where, $\boldsymbol{w}$, $\boldsymbol{v}$ are the input and output white noises with covariance $\boldsymbol{Q}_{\mathrm{WV}}$. The cost function in LQG is formulated as the expectation of the objective similar to those in LQR.

$$J = \mathrm{E}\left\{\lim_{\tau\to\infty}\frac{1}{\tau}\int_0^{\tau}\left([\boldsymbol{x}^{\mathrm{T}} \quad \boldsymbol{u}^{\mathrm{T}}]\boldsymbol{Q}_{\mathrm{XU}}\begin{bmatrix}\boldsymbol{x}\\ \boldsymbol{u}\end{bmatrix} + \boldsymbol{x}_{\mathrm{i}}\boldsymbol{Q}_{\mathrm{i}}\boldsymbol{x}_{\mathrm{i}}\right)\mathrm{d}t\right\} \quad (32)$$

where $\boldsymbol{x}_i$ is the integral of the tracking error, $\boldsymbol{Q}_{\mathrm{XU}}$ and $\boldsymbol{Q}_{\mathrm{i}}$ are the controller parameters.

Two degrees of freedom of LQG controllers are designed for both longitudinal and lateral motions subject to the specific controller parameters $\boldsymbol{Q}_{\mathrm{XU}}$, $\boldsymbol{Q}_{\mathrm{WV}}$ and $\boldsymbol{Q}_{\mathrm{i}}$. Studies are composed of longitudinal control and lateral control. In this paper, we focus on the attitude control of HARW, that is, the inner loop controller design.

4.3.1. Longitudinal dynamics control

For longitudinal controller design, flexibility may be neglectable under small deformation, as shown in Fig. 12. Nevertheless, if not considered under large deformation, the coupling of rigid body motion and structural movement will deteriorate the control effect, and the rigid body state vibrates for a very long time under the influence of structure states in Fig. 13. Besides, deviation of the longitudinal state causes slight lateral motion.

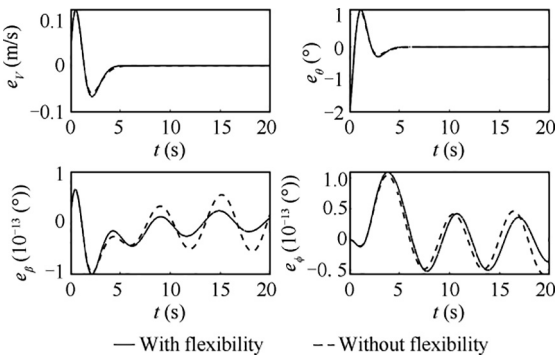

Fig. 12 Historical trajectories of deviation of pitch angle in closed-loop simulation for HARW with empty load.

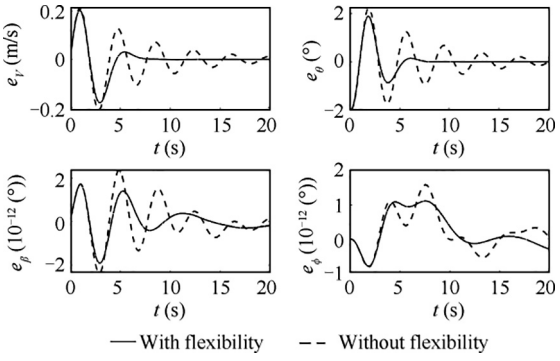

Fig. 13 Historical trajectories of deviation of pitch angle in closed-loop simulation for HARW with full load.

4.3.2. Lateral attitude control

The responses of deviation of roll angle of empty and full load with different controllers are given in Fig. 14 and Fig. 15. For lateral controller design, flexibility needs to be considered both under small deformation and large deformation. The lateral controller without flexibility diverges because of the model uncertainties. The settling time is long for HARW, and the coupling between lateral and structural motion is more substantial than between longitudinal and structural motion. Besides, large longitudinal motion will be generated both in

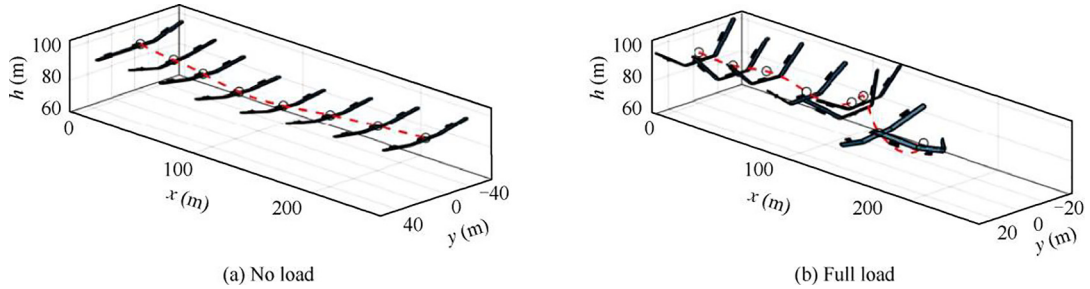

Fig. 11 3D simulation of nonlinear dynamic of HARW with different deformation.

Fig. 14 and Fig. 15. Therefore, lateral stability is more critical for HARW.

Although ailerons can control the dihedral angle, we found that the performance of the controller improves with the dihedral angle controlled. However, the difficulty of control implementation increases essentially. For the HARW model in this paper, it is better not to actively control the structural motion.

4.3.3. Steady control with gust disturbance

The large deformation makes HARW unstable. When disturbed by a gust, the aircraft will diverge. Significant changes in structure can cause the aircraft to break down. The Dryden and Von Karman gust models are the classical approaches to describing atmosphere turbulence using the Power Spectral Density (PSD) functions. The gust generated is then transformed into velocity, AOA and AOS disturbance to fit the proposed model. The transformed gust turbulence is shown below in Fig. 16.

Fig. 17 shows the controlled states and inputs response with the gust turbulence for the 40 s. The LQG controller considering flexible states can stabilize the system effectively. Besides, trajectory control is necessary when encountering gust disturbance.

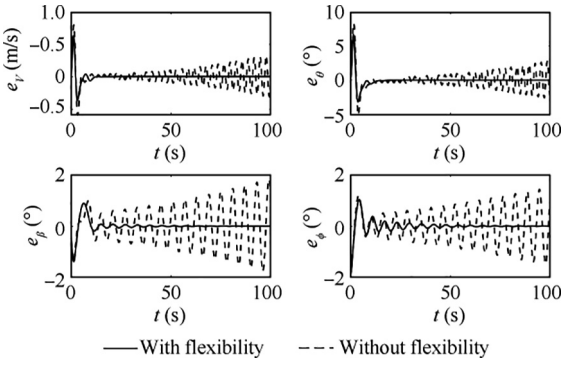

Fig. 14 Historical trajectories of deviation of roll angle in closed-loop simulation for HARW with empty load.

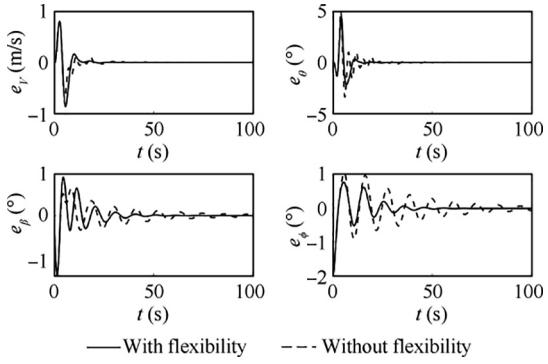

Fig. 15 Historical trajectories of deviation of roll angle in closed-loop simulation for HARW with full load.

5. Conclusions

(1) A Control-Oriented Model (COM) of six-DOF dynamics for a High-Aspect-Ratio Wing (HARW) is developed in this paper. Compared with the flight dynamics characteristics observed in the higher fidelity model of HARW, the COM captures the critical characteristics, including the unstable phugoid, the merge of a pair of complex-conjugate short-period to two real roots. What's more, other features are obtained based on the COM.

(2) The loss of lift due to the unsteady effects of dihedral angles mainly accounts for the non-minimum phase behaviour in flight path angle tracking, which introduces a single positive real transmission zero with the given control input.

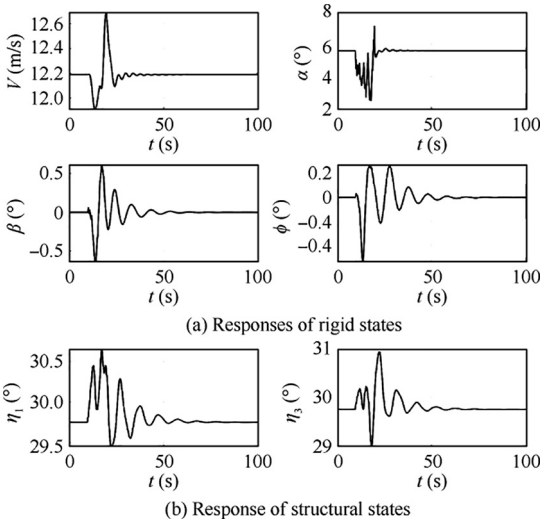

Fig. 17 Responses with gust excitation.

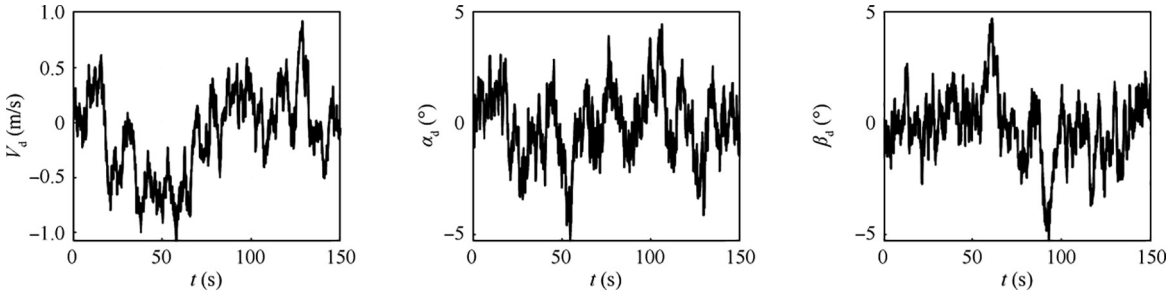

Fig. 16 Examples of von Karmen gust profile.

(3) The interaction for longitudinal channel input is weakened, whereas lateral channel input is raised as the deformation goes large. The damping of the short-period mode is driven by the moment of inertia. The longitudinal and lateral modes of HARW can be physically decoupled under specific flight conditions.
(4) The COM must be further modified with experimental or high-precision theoretical models in future studies. The robust control approach will be attempted because the model is sensitive to uncertainties.

Declaration of Competing Interest

The authors declare that they have no known competing financial interests or personal relationships that could have appeared to influence the work reported in this paper.

Acknowledgements

This study was co-supported by the Natural Science Foundation of Jiangsu Province, China (No. BK20200437), the National Natural Science Foundation of China (No. 62103187) and the Fundamental Research Funds for the Central Universities, China (No. NT2022025).

Appendix A.

See Table A1–A7

Table A1 Coefficients of CFM for C_L.

Load	Coefficients					
	C_L^0	C_L^α	$C_L^{\dot{\eta}_s}$	$C_L^{\delta_e^s}$	$C_L^{\delta_a^c}$	$C_L^{\delta_a^d}$
EL	0.02	19.85	−1.49	1.18	3.07	1.02
FL	0.00	17.14	−2.41	1.11	2.80	0.92

Table A2 Coefficients of CFM for C_D.

Load	Coefficients			
	C_D^0	κ_D	$C_D^{\dot{\eta}_{as}p}$	$C_D^{p^2}$
EL	0.10	0.02	−14.57	−30.37
FL	0.12	0.02	−13.19	−24.77

Table A3 Coefficients of CFM for C_Y.

Load	Coefficients					
	C_Y^β	$C_Y^{\eta_{as}}$	$C_Y^{p\eta_s}$	$C_Y^{\eta_s\dot{\eta}_{as}}$	$C_Y^{\delta_a^d}$	$C_Y^{\delta_e^{as}}$
EL	−0.57	0.54	−13.71	−3.44	0.15	0.13
FL	−3.16	0.24	−11.45	−2.87	0.49	0.38

Table A4 Coefficients of CFM for C_l.

Load	Coefficients				
	C_l^β	C_l^p	$C_l^{\dot{\eta}_{as}}$	$C_l^{\delta_e^{as}}$	$C_l^{\delta_a^d}$
EL	−21.19	−275.30	−70.46	8.31	9.92
FL	−58.98	−215.64	−55.01	7.00	9.12

Table A5 Coefficients of CFM for C_m.

Load	Coefficients					
	C_m^0	C_m^α	$C_m^{\dot{\eta}_s}$	$C_m^{\delta_e^s}$	$C_m^{\delta_a^c}$	$C_m^{\delta_a^d}$
EL	0.07	−7.44	0.55	−3.81	−1.21	−0.44
FL	0.04	−6.62	1.49	−3.52	−1.20	−0.41

Table A6 Coefficients of CFM for C_n.

Load	Coefficients				
	C_n^{β}	$C_n^{\alpha p}$	$C_n^{\alpha \dot{\eta}_{as}}$	C_n^{r}	$C_n^{\alpha \delta_e^{as}}$
EL	−2.03	−296.23	−72.69	−4.10	−3.59
FL	−3.06	−184.14	−52.39	−3.46	−8.79

Table A7 Coefficients of CFM for C_{hi}.

Load	Coefficients									
	C_{hi}^{0}	C_{hi}^{α}	C_{hi}^{β}	C_{hi}^{p}	$C_{hi}^{\dot{\eta}_i}$	$C_{hi}^{\delta_a^c}$	$C_{hi}^{\delta_{ai}^d}$	$C_{hi}^{\delta_e^{as}}$	$C_{hi}^{\delta_e^d}$	$C_{hi}^{\delta_e^s}$
EL	±4.77	∓82.48	−13.65	−172.32	−65.28	∓13.17	∓12.32	4.84	∓0.87	∓3.73
FL	±4.41	∓73.62	−42.67	−148.29	−64.66	∓13.01	∓12.26	4.8	∓1.07	∓4.05

References

1. Afonso F, Vale J, Oliveira É, et al. A review on non-linear aeroelasticity of high aspect-ratio wings. *Prog Aeros Sci* 2017;**89**:40–57.
2. Noll T, Brown J, Perez-Davis M, et al. Investigation of the Helios prototype aircraft mishap volume I mishap report; 2004. Washington, D.C.: NASA Langley Research Center; Report No.: 64317.
3. Cesnik C, Hodges D, Patil M. Aeroelastic analysis of composite wings*37th structure, structural dynamics and materials conference; 1996 Apr 15–17; Salt Lake City*. Reston: USA: AIAA; 1996.
4. van Schoor MC, von Flotow AH. Aeroelastic characteristics of a highly flexible aircraft. *J Aircr* 1990;**27**(10):901–8.
5. Babcock J, Lind R. Aeroelastic effects of battens on the flight dynamics of a MAV*AIAA atmospheric flight mechanics conference; 2012 Aug* 13–16; Minneapolis. USA. Reston: AIAA; 2012.
6. Lei H, Chen BY, Liu YB, et al. Modified Kalman particle swarm optimization: application for trim problem of very flexible aircraft. *Eng Appl Artif Intell* 2021;**100**:104176.
7. Patil MJ, Hodges DH. Flight dynamics of highly flexible flying wings. *J Aircr* 2006;**43**(6):1790–9.
8. Johnson M. Finite-state airloads for deformable airfoils on fixed and rotating wings [dissertation]. Washington, D.C.: University in St. Louis; 1995.
9. Peters DA, Karunamoorthy S, Cao WM. Finite state induced flow models. I – Two-dimensional thin airfoil. *J Aircr* 1995;**32**(2):313–22.
10. Cesnik C, Brown E. Modeling of high aspect ratio active flexible wings for roll control*43rd AIAA, ASME, ASCE, AHS, ASC structures, structural dynamics, and materials conference;* 2002 Apr 22–25; Denver, USA. Reston: AIAA; 2002.
11. Xie CC, Yang L, Liu Y, et al. Stability of very flexible aircraft with coupled nonlinear aeroelasticity and flight dynamics. *J Aircr* 2017;**55**(2):862–74.
12. Lei H, Xu L, Chen BY, et al. Comparison of model reduction methods for very flexible aircraft. *2018 33rd youth academic annual conference of Chinese association of automation (YAC);* Portland, Nanjing, China. Piscataway: IEEE Press; 2018. p. 450–5.
13. Nguyen NT, Reynolds K, Ting E, et al. Distributed propulsion aircraft with aeroelastic wing shaping control for improved aerodynamic efficiency. *J Aircr* 2018;**55**(3):1122–40.
14. Meirovitch L, Tuzcu I. Unified theory for the dynamics and control of maneuvering flexible aircraft. *AIAA J* 2004;**42**(4):714–27.
15. Dillsaver M, Cesnik C, Kolmanovsky I. Gust load alleviation control for very flexible aircraft. *AIAA atmospheric flight mechanics conference;* 2011 Aug 08–11. USA. Reston: AIAA; 2011. p. 2011.
16. Sadat-Hoseini H, Fazelzadeh SA, Rasti A, et al. Final approach and flare control of a flexible aircraft in crosswind landings. *J Guid Control Dyn* 2013;**36**(4):946–57.
17. Dillsaver M, Cesnik CE, Kolmanovsky I. Trajectory control of very flexible aircraft with gust disturbance. *AIAA atmospheric flight mechanics (AFM) conference;* Boston, USA. Reston: AIAA; 2013.
18. Qi PY, Zhao XW, Wang YN, et al. Aeroelastic and trajectory control of high altitude long endurance aircraft. *IEEE Trans Aeros Electron Syst* 2018;**54**(6):2992–3003.
19. Wang YN, Wynn A, Palacios R. Nonlinear aeroelastic control of very flexible aircraft using model updating. *J Aircr* 2018;**55**(4):1551–63.
20. Shearer CM, Cesnik CES. Trajectory control for very flexible aircraft. *J Guid Control Dyn* 2008;**31**(2):340–57.
21. Gregory I. Stability result for dynamic inversion devised to control large flexible aircraft. *AIAA guidance, navigation, and control conference and exhibit;* 2001 Aug 06–09; Canada. Reston: AIAA; 2001.
22. Raghavan B, Patil MJ. Flight control for flexible, high-aspect-ratio flying wings. *J Guid Control Dyn* 2010;**33**(1):64–74.
23. Chen J, Freudenberg JS, Nett CN. The role of the condition number and the relative gain array in robustness analysis. *Automatica* 1994;**30**(6):1029–35.
24. Patil MJ, Hodges DH. Output feedback control of the nonlinear aeroelastic response of a slender wing. *J Guid Control Dyn* 2002;**25**(2):302–8.
25. Cook RG, Palacios R, Goulart P. Robust gust alleviation and stabilization of very flexible aircraft. *AIAA J* 2013;**51**(2):330–40.
26. Qu Z, Annaswamy AM. Adaptive output-feedback control with closed-loop reference models for very flexible aircraft. *J Guid Control Dyn* 2015;**39**(4):873–88.
27. Kumar M, Balakrishnan SN. Proper orthogonal decomposition technique for sub-optimal control of flexible aircraft wings using discrete actuators. 2014 American control conference; 2014 Jun 4–6; Portland, USA. Piscataway: IEEE Press; 2014. p. 2717–22.
28. Parker JT, Serrani A, Yurkovich S, et al. Control-oriented modeling of an air-breathing hypersonic vehicle. *J Guid Control Dyn* 2007;**30**(3):856–69.
29. Santina CD, Rus D. Control oriented modeling of soft robots: the polynomial curvature case. *IEEE Robotics Autom Lett* 2020;**5**(2):290–8.

30. Chen BY, Shen HD, Lei H. Sensitivity analysis of performance for control-oriented model of an air-breathing hypersonic vehicle*21st AIAA international space planes and hypersonics technologies conference;* 2017 Mar 6–9; China. Reston: AIAA; 2017. p. 2017.
31. Chen BY, Liu YB, Shen HD, et al. Performance limitations in trajectory tracking control for air-breathing hypersonic vehicles. *Chin J Aeronaut* 2019;**32**(1):167–75.
32. Gibson T, Annaswamy A, Lavretsky E. Modeling for control of very flexible aircraft. *AIAA guidance, navigation, and control conference;* 2011 Aug 08-11. USA. Reston: AIAA; 2011. p. 2011.
33. Skogestad S, Postlethwaite I. *Multivariable feedback control: analysis and design*. New York: Wiley; 2007.
34. Raghavan B. Flight dynamics and control of highly flexible flying-wings [dissertation]. Blacksburg: Virginia Polytechnic Institute and State University; 2009.